

# Deciphering CO oxidation on SnO<sub>2</sub> nanosheets: A multinuclear solid-state NMR spectroscopic approach

Xiang Wang,<sup>a,b</sup> Guodong Qi,<sup>a,\*</sup> Qiang Wang,<sup>a</sup> Jun Xu,<sup>a,\*</sup> and Feng Deng<sup>a</sup>

<sup>a</sup>National Center for Magnetic Resonance in Wuhan, State Key Laboratory of Magnetic Resonance and Atomic and Molecular Physics, Wuhan Institute of Physics and Mathematics, Innovation Academy for Precision Measurement Science and Technology, Chinese Academy of Sciences, Wuhan, 430071, P. R. China

<sup>b</sup>University of Chinese Academy of Sciences, Beijing, 100049, P. R. China

Email: [gqdong@wipm.ac.cn](mailto:gqdong@wipm.ac.cn); [xujun@wipm.ac.cn](mailto:xujun@wipm.ac.cn)

Dedicated to Prof. Graham Hutchings on his 70th birthday

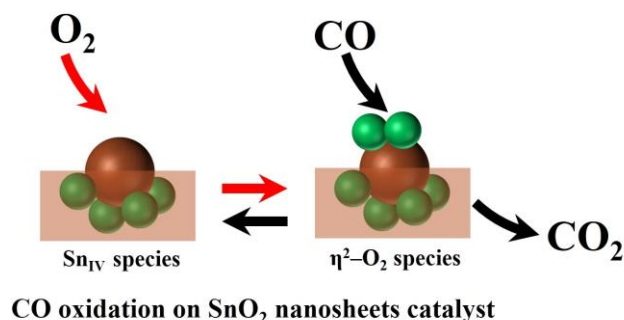
Received 12-15-2023

Accepted Manuscript 02-07-2024

Published on line 02-16-2024

## Abstract

SnO<sub>2</sub> nanosheets exhibit exceptional low-temperature CO oxidation activity, yet the nature of their active sites remains enigmatic. Employing solid-state <sup>119</sup>Sn and <sup>17</sup>O NMR spectroscopy, we deconstructed the intricate structure of active Sn and oxygen species involved in this process. We identified diverse Sn and O environments, revealing surface Sn<sub>IV</sub> sites capable of activating O<sub>2</sub> into a critical bidentate η<sup>2</sup>-O<sub>2</sub> species responsible for CO conversion into CO<sub>2</sub>. In-situ FT-IR spectroscopy studies further revealed the involvement of a carbonate-mediated Mars-van Krevelen mechanism.



**Keywords:** CO oxidation, SnO<sub>2</sub> nanosheets, active sites, mechanism, NMR spectroscopy

## Introduction

As a toxic gas, carbon monoxide (CO) poses risks to human health and the environment. It is commonly found in automobile and factory exhaust gases due to widespread reliance on fossil fuels for energy. It is essential to eliminate CO, especially in confined spaces such as submarines and aerospace stations.<sup>1-3</sup> Among various processes for CO elimination, catalytic oxidation is the most effective approach. Precious metals such as Au,<sup>4-6</sup> Pt,<sup>7-10</sup> and Pd<sup>11, 12</sup> exhibit excellent activity for catalyzing CO oxidation at low temperatures. However, large-scale applications of noble metal catalysts are limited by their scarce reserves and high costs. Therefore, non-precious metal catalysts with abundant reserves and lower costs need to be developed instead.<sup>13</sup> By synthesizing or constructing coordination unsaturated metal active sites,<sup>14-19</sup> such as Fe, Co, Ni, Cu, Zr, Zn, Sn Mn or Mo, non-precious metal catalysts can achieve remarkable catalytic reactivity due to electron transfer between the vacant orbitals of these metal atoms and the reactant molecules. For example, coordination unsaturated Co<sup>3+</sup> sites on cobalt oxide nanorods can catalyze CO oxidation extremely effectively, even at low temperatures like 196 K.<sup>20</sup> Moreover, monovalent zinc sites confined in zeolite channels can activate molecular oxygen via a single electron transfer mechanism to produce superoxide species, promoting catalytic CO oxidation at room temperature.<sup>21</sup> In addition, coordinatively unsaturated Fe<sup>2+</sup> confined on Pt nanoparticle surfaces displays high efficiency and selectivity for CO oxidation under hydrogen-rich conditions used in proton-exchange membrane fuel cells.<sup>22</sup>

Tin oxide (SnO<sub>2</sub>) with various nanostructures, such as spheres, rods and sheets, has been widely applied in numerous areas including gas sensing,<sup>23</sup> catalysis<sup>24-27</sup> and water photolysis.<sup>28</sup> Regarding catalytic CO oxidation, the reactivity of SnO<sub>2</sub> follows this order: nano-sheets<sup>29,30</sup> > nano-rods<sup>31</sup> > nano-spheres<sup>29</sup>. Therefore, synthesizing SnO<sub>2</sub> nanosheets is a promising approach to improve the CO oxidation activity of SnO<sub>2</sub>-based catalysts. However, due to the structural complexity of nano-SnO<sub>2</sub>, identifying the structure of active Sn sites and understanding their roles in CO oxidation remain challenging. Hence, the characterization of the active Sn species and elucidating their functions in catalytic reactions, are not only fundamentally important, but also critical for developing efficient nano-SnO<sub>2</sub> catalysts.

Solid-state nuclear magnetic resonance (NMR) spectroscopy has emerged as a powerful technique to provide molecular-level information about active-site structures and their dynamics in heterogeneous catalysis.<sup>32-34</sup> Sn has two NMR spectroscopy-active isotopes, <sup>117</sup>Sn and <sup>119</sup>Sn, which are both spin 1/2 nuclei with relatively high gyromagnetic ratios ( $-9.59 \times 10^7 \text{ rad} \cdot \text{s}^{-1} \cdot \text{T}^{-1}$  for <sup>117</sup>Sn and  $-10.03 \times 10^7 \text{ rad} \cdot \text{s}^{-1} \cdot \text{T}^{-1}$  for <sup>119</sup>Sn) and natural abundance (7.67% for <sup>117</sup>Sn and 8.58% for <sup>119</sup>Sn). Of note is that <sup>119</sup>Sn is commonly used in NMR spectroscopy studies because it has higher sensitivity than <sup>117</sup>Sn.<sup>35</sup> Harris and co-workers initiated the solid-state NMR spectroscopic studies of Sn,<sup>36-39</sup> while the first solid state Sn NMR spectrum of SnO<sub>2</sub> was reported by Cossement and co-workers in 1992.<sup>40</sup> In 2016, Chen *et al.* demonstrated that solid-state <sup>119</sup>Sn NMR spectroscopy could be employed to monitor the surface structure of nano-sized SnO<sub>2</sub>.<sup>41</sup> <sup>119</sup>Sn NMR spectroscopic chemical shifts were demonstrated to be able to distinguish Sn atoms in the first, second and bulk layers of nanosheets and their evolution during reactions. Our recent work showed that the proton-detected 2D <sup>1</sup>H {<sup>119</sup>Sn} correlation solid-state NMR spectroscopy provides strong evidence for Sn species with Sn-OH structure on zeolites.<sup>42</sup> On the other hand, solid-state <sup>17</sup>O NMR spectroscopy is frequently employed to study local structures and oxygen environments,<sup>43,44</sup> although this technique has low sensitivity and complex line shapes due to the intrinsic properties of <sup>17</sup>O, e.g. small gyromagnetic ratio, low natural abundance and moderate quadrupole moment. In 2017, Peng and co-workers used solid-state <sup>17</sup>O NMR spectroscopy to study the oxygen species on anatase titania nanocrystals with different facets, finding that oxygen ions on the exposed (001) and (101) facets exhibited distinct <sup>17</sup>O chemical shifts sensitive to the nanocrystals' surface

properties.<sup>45</sup> These solid-state NMR spectroscopy studies offered viable approaches for characterizing metal oxides and related materials. Therefore, combining solid-state  $^{119}\text{Sn}$  and  $^{17}\text{O}$  NMR spectroscopy could provide a comprehensive characterization of active metal sites by helping to elucidate their roles in the activation of oxygen during catalytic applications.

In this work, we demonstrate a multinuclear solid-state NMR spectroscopic approach to study the mechanism of low temperature CO oxidation on atomically-thin 2D  $\text{SnO}_2$  nanosheets synthesized by a solvothermal method.<sup>30</sup> Furthermore, solid-state  $^{119}\text{Sn}$  NMR spectroscopy helped identify the coordinatively unsaturated tetrahedral Sn sites serving as the active sites for gas oxygen activation. Lastly, solid-state  $^{17}\text{O}$  NMR spectroscopy was applied to determine the active oxygen species generated on these active tin sites. Through the combination of these techniques, the pathway of gas oxygen activation and the mechanism of CO oxidation over this material was thus revealed.

## Results and Discussion

### Synthesis and catalytic activity of $\text{SnO}_2$ Nanosheets for CO oxidation

The  $\text{SnO}_2$  nanosheets were prepared via a previously reported solvothermal synthesis method.<sup>30</sup> Scanning electron microscopy (SEM) and transmission electron microscopy (TEM) images (Figure 1a and 1b) reveal the nanosheet morphology of the obtained  $\text{SnO}_2$  catalyst. The X-ray diffraction (XRD) pattern (Figure 1c) confirmed the pure rutile  $\text{SnO}_2$  with a tetragonal structure (JCPDS no. 00-041-1445), consistent with previous reports.<sup>30,41</sup> These characterization data provide reliable evidence of the successful synthesis of the atomically thin 2D  $\text{SnO}_2$  nanosheets.

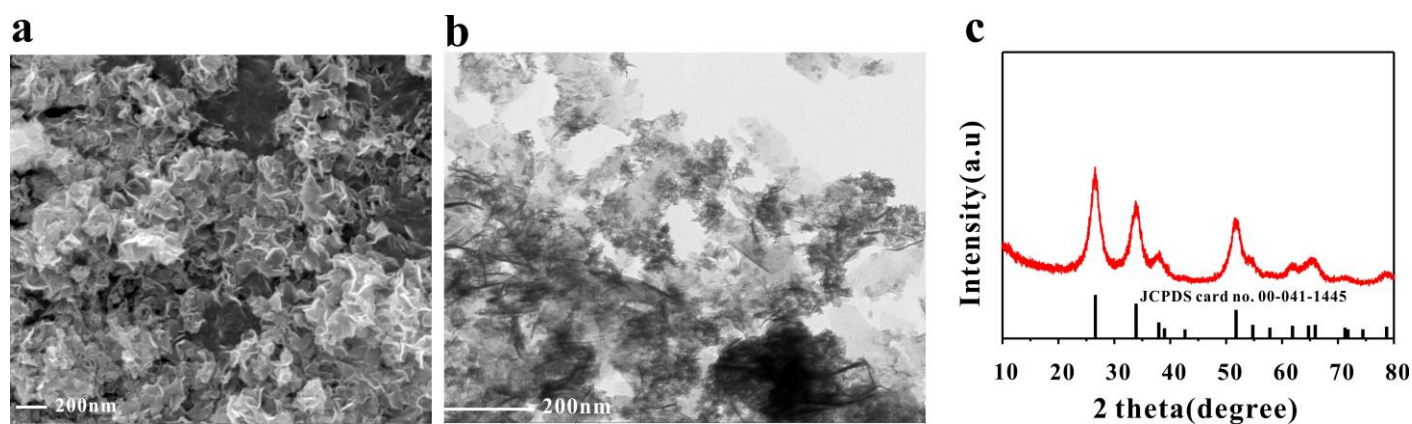


**Figure 1.** SEM image (a), TEM image (b) and XRD pattern (c) of the synthesized  $\text{SnO}_2$  catalyst.

The catalytic performance of the  $\text{SnO}_2$  nanosheets for CO oxidation was evaluated next. Figure 2 shows the CO conversion at different reaction temperatures for the  $\text{SnO}_2$  nanosheets, before and after reduction with CO. The  $\text{SnO}_2$  nanosheets pre-treated with CO demonstrate higher CO oxidation activity compared to the as-synthesized sample (Figure 2a), as evidenced by a much lower  $T_{50}$  value (the temperature required to achieve 50% CO conversion) of 128°C for the CO-reduced catalyst versus 283°C for the untreated catalyst. The low-temperature activity of the CO-reduced catalyst is maintained in the first and second reaction cycles, but deactivation occurs in the third cycle (Figure 2b). These results indicate that CO reduction significantly

influences the CO oxidation activity of the SnO<sub>2</sub> nanosheets, suggesting the presence of different active sites or a “changing of availability” for active sites on the catalysts, before and after CO reduction treatment.

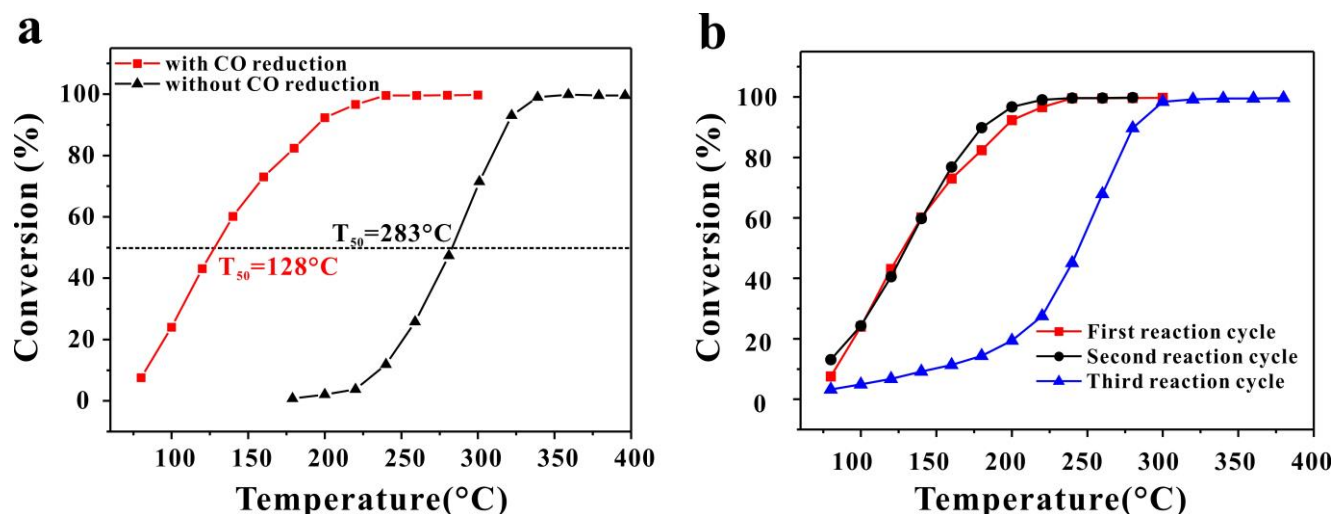


**Figure 2.** Light-off curves of CO oxidation on the SnO<sub>2</sub> nanosheets, with and without CO reduction (a) and CO conversion on CO-reduced SnO<sub>2</sub> nanosheets at 75 to 400 °C with one to three times reaction cycles (b).

### Solid state NMR spectroscopy analysis of active Sn sites

Solid-state <sup>119</sup>Sn magic-angle-spinning (MAS) NMR spectroscopy experiments were carried out on the as-synthesized and CO-reduced SnO<sub>2</sub> nanosheets in order to characterize the active Sn sites (Figure 3a and 3b). Four distinct Sn sites were observed with chemical shifts at -568, -586, -604, and -618 ppm in the spectra of both samples. After careful signal simulation, the relative proportions of these signals was obtained as listed in Table 1, entries 1 and 2. Comparing the changes before and after the first CO reduction revealed a significant decrease (from 84.8% to 50.5%) in the strongest signal at -604 ppm, assigned to hexacoordinated Sn (Sn<sub>VI</sub>) sites on SnO<sub>2</sub> samples.<sup>40,41</sup> Meanwhile, the proportion of Sn sites at -586 ppm increased from 8.5% to 42.9%. Notably, the increase in -586 ppm Sn sites directly corresponded to the decrease in -604 ppm Sn<sub>VI</sub> sites. The -586 ppm Sn sites likely represents coordination-unsaturated Sn species resulting from CO reduction of Sn<sub>VI</sub> sites.<sup>46,47</sup> Additionally, the 42.9% proportion of -586 ppm Sn sites on the CO-reduced sample agreed well with the previously reported 40% proportion of surface tetracoordinated Sn (Sn<sub>IV</sub>) sites on SnO<sub>2</sub> nanosheets.<sup>30</sup> Therefore, we hypothesize that upon exposure to air during preparation, the majority of the surface Sn<sub>IV</sub> sites on the as-synthesized SnO<sub>2</sub> nanosheets become saturated to Sn<sub>VI</sub> sites coordinated with oxygen.

To verify this hypothesis, oxygen gas was introduced onto the CO-reduced sample after heating it to 220°C, and the solid-state <sup>119</sup>Sn MAS NMR spectrum was recorded (Figure 3c) and analyzed (Table 1, entry 3). As expected, a reduction in Sn<sub>IV</sub> at -586 ppm, accompanied by an almost equivalent increase in Sn<sub>VI</sub> at -604 ppm, was observed, suggesting the reversible transformation between surface Sn<sub>IV</sub> and Sn<sub>VI</sub> sites. The interconversion between Sn<sub>IV</sub> and Sn<sub>VI</sub> was also confirmed by recovering the Sn<sub>IV</sub> sites when a second CO reduction was applied to the sample after oxidation with O<sub>2</sub> (Figure 3d and Table 1, entry 4). The active role of surface Sn<sub>IV</sub> sites is demonstrated by their decrease and growth upon O<sub>2</sub> oxidation and CO reduction, respectively. Meanwhile, a loss of active Sn<sub>IV</sub> sites was observed when comparing the amounts after the first and second CO reductions (Figure 3b and 3d and Table 1, entries 2 and 4), and was found to be consistent with catalyst deactivation in repeat runs (Figure 2b). The proportions of Sn sites at -568 ppm and -618 ppm remained almost unchanged at low levels, regardless of reductive or oxidative treatment. This implied that

these Sn sites are probably “spectators” during the CO oxidation process, likely representing sub-surface Sn<sub>IV</sub> and Sn<sub>VI</sub> sites whose reduction and oxidation characteristics are inhibited by surface Sn species.

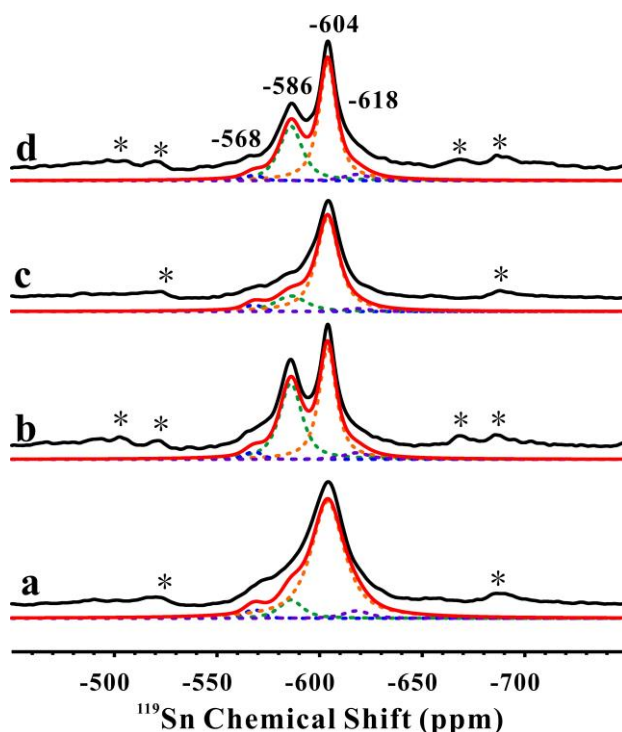


**Figure 3.**  $^{119}\text{Sn}$  MAS NMR spectra of the as-synthesized  $\text{SnO}_2$  nanosheets (a), sample (a) with the first CO-reduction at  $220^\circ\text{C}$  (b), sample (b) with  $\text{O}_2$  oxidation at  $220^\circ\text{C}$  (c), and sample (c) with the second CO-reduction at a higher temperature ( $280^\circ\text{C}$ ) (d). The experimental, simulated and deconvolved spectra for each tin sites are represented by solid black lines, solid red lines and colored dash lines, respectively.

**Table 1.** Quantitative analysis of Sn sites on  $\text{SnO}_2$  nanosheets with different treatments based on  $^{119}\text{Sn}$  MAS NMR spectroscopy

SnO <sub>2</sub> nanosheets	The proportion of Sn sites at different chemical shift (%)			
	-568 ppm	-586 ppm	-604 ppm	-618 ppm
As-synthesized	2.5	8.5	84.8	4.2
First CO-reduction	2.5	42.9	50.5	4.1
O <sub>2</sub> -oxidized	2.3	17.6	76.3	3.8
Second CO-reduction	2.4	34.3	59.2	4.1

### O<sub>2</sub> activation on the coordination-unsaturated Sn sites

Solid-state  $^{17}\text{O}$  MAS NMR spectroscopy experiments were employed to explore the interaction between  $\text{O}_2$  and the coordination-unsaturated surface Sn<sub>IV</sub> sites, key to understanding the oxidation mechanism. Experiments were performed at 18.8T with fast 35 kHz MAS for high spectral resolution. Figure 4a shows  $^{17}\text{O}$  MAS NMR spectra after introducing  $^{17}\text{O}_2$  onto  $\text{SnO}_2$  nanosheets with different pretreatments. Upon heating  $^{17}\text{O}_2$ -exposed CO-pretreated nanosheets to  $220^\circ\text{C}$ , a broad weak singal at 238 ppm, a narrow singal at 137 ppm and overlapping resonances from 0-100 ppm are resolved. 2D  $^1\text{H}\{-^{17}\text{O}\}$  direct heteronuclear multiple quantum coherence (D-HMQC) NMR spectroscopy was subsequently performed to allow for preliminary signal



assignments. As Figure 5 shows,  $^1\text{H}$ - $^{17}\text{O}$  correlations at (5.8, 56), (1.6, 46) and (-0.5, 9) ppm are likely assigned to water-adsorbed, bridging and terminal Sn-OH groups, respectively.<sup>48</sup> Identifying  $^{17}\text{O}$  chemical shifts of Sn-OH groups allowed for the resolution of overlapping resonances (0-100 ppm) by considering isotropic shifts and quadrupole parameters. Besides the three defined OH groups, two signals at 92 and 21 ppm were identified. Site proportions are listed in Table 2, entry 1. To determine the O sites involved in CO oxidation, the  $^{17}\text{O}_2$ -exposed sample (Figure 4a) was reacted with CO at 120 °C near its  $T_{50}$  temperature, and examined by  $^{17}\text{O}$  MAS NMR spectroscopy (Figure 4b, Table 2, entry 2). The site proportion at 21 ppm noticeably decreased relative to that in Figure 4a, decreasing from 1 to 0.62, while the proportions at other sites only changed slightly. The further  $^{17}\text{O}_2$  exposure of this CO-reacted sample at 220 °C (Figure 4c, Table 2, entry 3) resulted in the recovery of the 21 ppm site. This strongly suggests that the 21 ppm site serves as the active oxygen species for CO oxidation.

Combining the  $^{17}\text{O}$  and  $^{119}\text{Sn}$  MAS NMR spectroscopic results, different types of oxygen species on  $\text{SnO}_2$  nanosheets are proposed in Figure 6. The proposed process involves bidentate adsorption of gas  $\text{O}_2$  on surface  $\text{Sn}_{\text{IV}}$  sites, leaving an  $\eta^2\text{-O}_2$  species and producing  $\text{Sn}_{\text{VI}}$  sites. The formation of  $\eta^2\text{-O}_2$  species requires a two-electrons transformation from the metal to the adsorbed  $\text{O}_2$ , a process which is commonly found with metal oxides, such as  $\text{CeO}_2$ .<sup>49</sup> The proportions of 238 and 92 ppm oxygen sites continually increase with  $^{17}\text{O}_2$  oxidation, suggesting isotope exchange between surface  $^{17}\text{O}$  species and 3- or 2-coordinated oxygen in subsurface  $\text{SnO}_2$  nanosheet layers. Meanwhile, the 137 ppm oxygen proportion grows after the CO reaction, but reduces after  $^{17}\text{O}_2$  oxidation (Table 2), probably due to carbonate formation from the CO adsorption. Additionally, of note was that hydroxyl group proportions varied randomly with redox treatment, excluding them as active sites for CO oxidation.

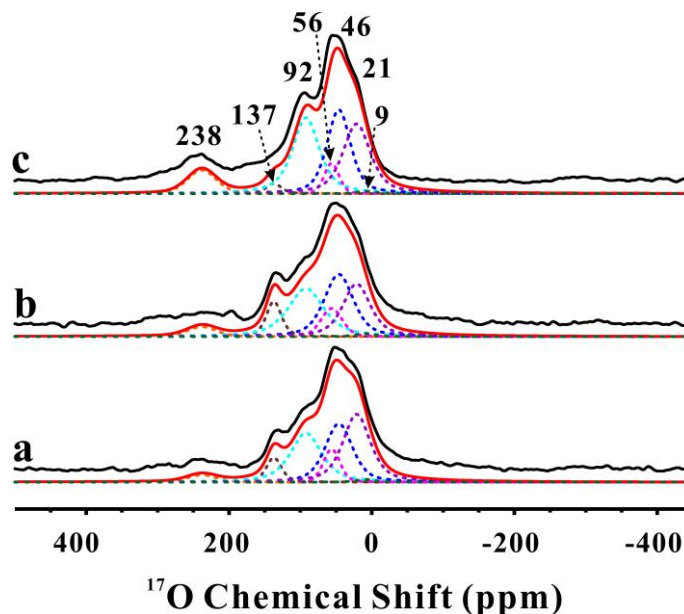


**Figure 4.**  $^{17}\text{O}$  MAS NMR spectra of the firstly CO-reduced  $\text{SnO}_2$  nanosheets after being oxidized by  $^{17}\text{O}_2$  at 220 °C (a), sample (a) reduced by CO at 120 °C (b) and sample (b) re-oxidized by  $^{17}\text{O}_2$  at 220 °C (c). The experimental spectra, simulated spectra and deconvoluted spectra for each oxygen sites are represented by solid black lines, solid red lines and colored dash lines, respectively.

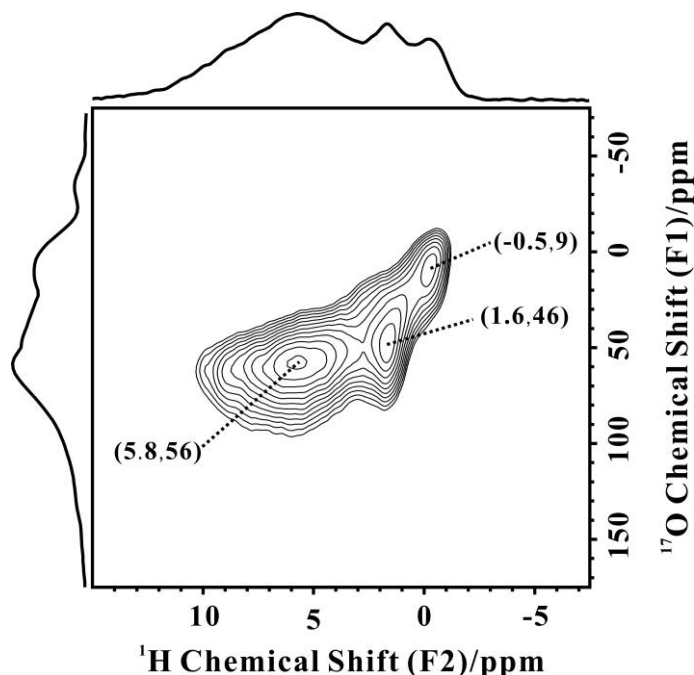


**Figure 5.** 2D  $^1\text{H}\{-^{17}\text{O}\}$  D-HMQC NMR spectrum of the firstly CO-reduced  $\text{SnO}_2$  nanosheets after being oxidized by  $^{17}\text{O}_2$  at 220  $^\circ\text{C}$ .

**Table 2.** Quantitative analysis of oxygen species on firstly CO-reduced  $\text{SnO}_2$  nanosheets after different treatments

Sample treatment	Oxygen species at different chemical shift <sup>a</sup>				
	238 ppm	137 ppm	92 ppm	The sum of 56, 46 and 9 ppm (hydroxyl groups)	21 ppm
$^{17}\text{O}_2$ -oxidation	0.10±0.01	0.19±0.01	0.85±0.01	1.13±0.02	1.00±0.01
CO-reduction	0.10±0.01	0.22±0.01	0.79±0.04	1.01±0.03	0.62±0.01
$^{17}\text{O}_2$ -re-oxidation	0.35±0.04	0.09±0.01	1.22±0.12	1.36±0.13	1.09±0.12

<sup>a</sup>Relative area compared to the reference signal at 21 ppm in Figure 4a. Error ranges were determined through triplicate deconvolution of each spectrum.

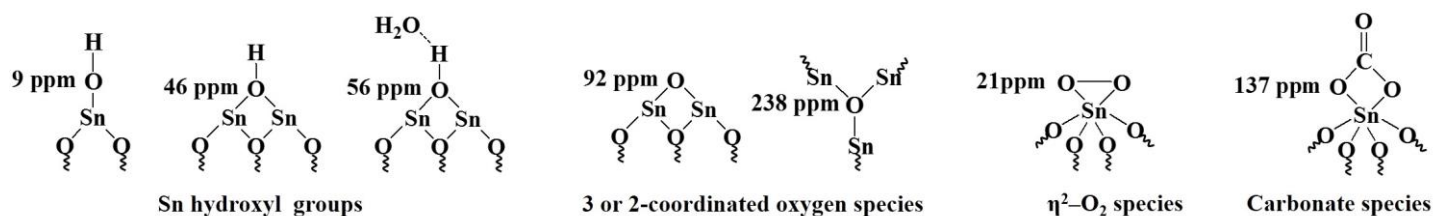


**Figure 6.** Proposed model of oxygen species produced by  $^{17}\text{O}_2$  activation on  $\text{SnO}_2$  nanosheets. The  $^{17}\text{O}$  NMR chemical shift are indicated in the left side of each oxygen sites.

### CO oxidation mechanisim catalyzed by coordinationally-unsaturated Sn sites

Several CO oxidation mechanisms have been proposed, including the Langmuir-Hinshelwood and Eley-Rideal pathways which differ in whether O<sub>2</sub> dissociates or reacts directly with CO.<sup>50</sup> These two mechanisms are often suggested on noble metal catalysts. The Mars-van Krevelen mechanism is accepted for metal oxide catalysts, where CO reacts with surface oxygen to form CO<sub>2</sub>, leaving oxygen vacancies. Molecular O<sub>2</sub> then replenishes the vacancies, recovering surface oxygen in one catalytic cycle.<sup>51</sup>

To gain insight into the CO oxidation mechanism over SnO<sub>2</sub> nanosheets, the reaction process was monitored via *in-situ* diffuse reflectance infrared Fourier transform spectroscopy (DRIFTS-FTIR) (Figure 7a and b). IR band intensities were used to analyze the evolution of CO<sub>2</sub> and carbonate species over reaction time (Figure 7c and d). As shown in Figure 7a and c, after introducing 5 kPa CO to pre-treated SnO<sub>2</sub> nanosheets (via CO reduction then O<sub>2</sub> oxidation), gradual growth of the CO<sub>2</sub> band (2310-2338 cm<sup>-1</sup>) and carbonate species bands (1600-1300 cm<sup>-1</sup>) which indicate CO oxidation occurs with increasing reaction time. Simultaneously, decreasing CO stretching bands (2114-2171 cm<sup>-1</sup>), which signify CO reactant consumption, are evident. After 20 min of reaction, the *in-situ* IR cell was evacuated and then charged with 5 kPa O<sub>2</sub>. Upon further heating for 20 min (Figure 7b and d), a continuous decrease of carbonate species was observed, accompanied by CO<sub>2</sub> formation. These results indicate the intermediate role of carbonate species during CO oxidation. The DRIFTS-FTIR spectroscopy analysis of the evolution of CO<sub>2</sub> and carbonate species showed analogous behavior to the oxygen sites observed at 137 ppm in <sup>17</sup>O MAS NMR, thus confirming the assignment of that chemical shift to the carbonate species. We are therefore able to conclude that CO oxidation over SnO<sub>2</sub> nanosheets follows a carbonate-mediated Mars-van Krevelen mechanism, as outlined graphically in Scheme 1. Specifically, coordination-unsaturated Sn<sub>IV</sub> sites interact with O<sub>2</sub> to form surface bidentate  $\eta^2$ -O<sub>2</sub> species on the surface of SnO<sub>2</sub> nanosheets (Step I). The bidentate  $\eta^2$ -O<sub>2</sub> species exhibit high reactivity with CO, facilitating the transformation to surface carbonate species (Step II). Dissociation of the surface carbonate species then produces CO<sub>2</sub> and a residual oxygen atom (Step III). The residual oxygen atom reacts with an additional CO molecule to yield further CO<sub>2</sub> (Step IV).<sup>52</sup> The catalytic cycle concludes upon regeneration of the coordinatively unsaturated Sn<sub>IV</sub> sites.

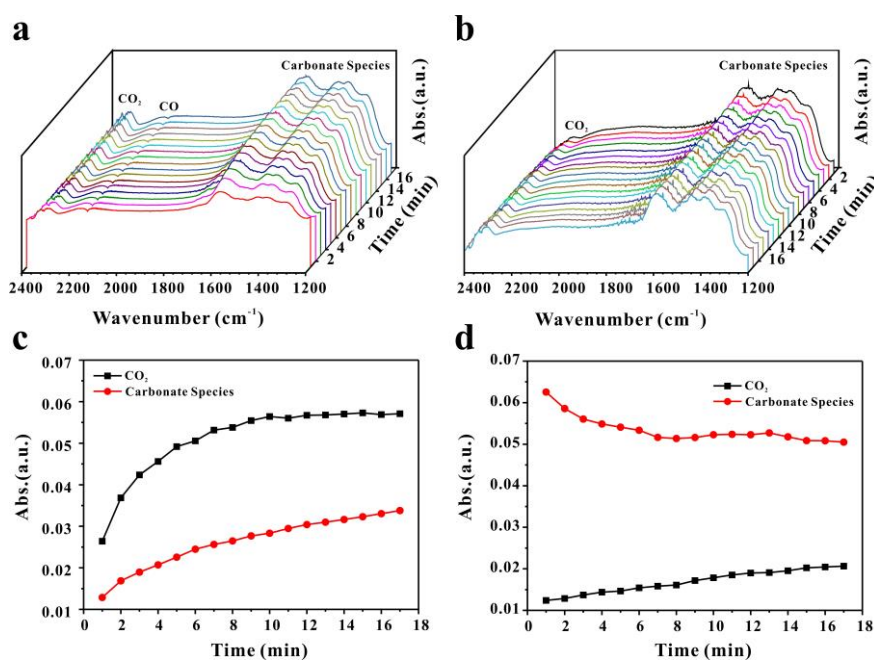
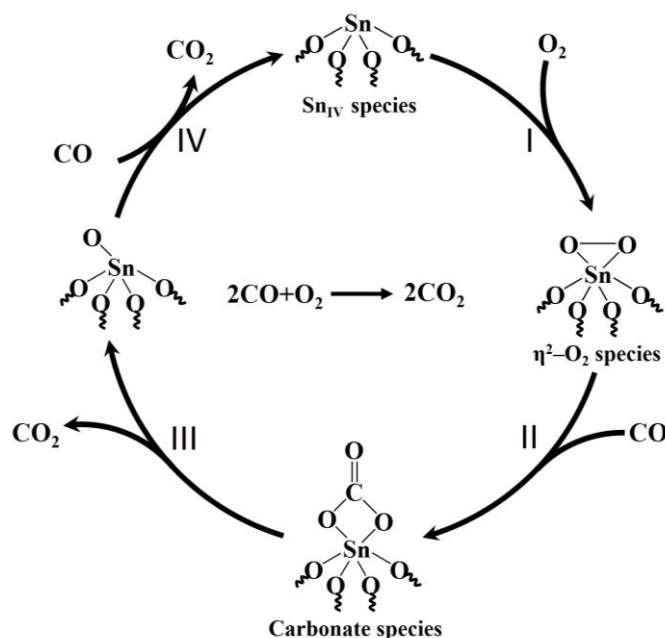


**Figure 7.** DRIFTS spectra and the evolution of CO<sub>2</sub> and carbonate species over time obtained from a CO (a, c) and O<sub>2</sub> (b, d) reaction cycle on SnO<sub>2</sub> nanosheets at 220 °C.





**Scheme 1.** Proposed catalytic pathway for the reaction of CO oxidation on SnO<sub>2</sub> nanosheets.

## Conclusions

By combining solid-state multinuclear NMR spectroscopy and *in-situ* DRIFTS, we have elucidated the detailed structure and dynamic behavior of active Sn and oxygen sites on SnO<sub>2</sub> nanosheets during low-temperature CO oxidation. <sup>119</sup>Sn NMR spectroscopy provides compelling evidence for the crucial role of surface Sn<sub>IV</sub> sites, undergoing reversible Sn<sub>IV</sub>-Sn<sub>VI</sub> interconversion upon O<sub>2</sub> capture and release, thus facilitating O<sub>2</sub> activation. Furthermore, <sup>17</sup>O NMR spectroscopy helped identify a bidentate η<sup>2</sup>-O<sub>2</sub> species on the surface Sn sites, generated via a postulated two-electron transfer between Sn<sub>IV</sub> and O<sub>2</sub>, as the key active oxygen species. Integrating these findings with *in-situ* DRIFTS data, we thus reveal evidence for a carbonate-mediated Mars-van Krevelen mechanism for CO oxidation on SnO<sub>2</sub> nanosheets. These results not only deepen our understanding of the catalytic mechanism on nano tin oxides, but also offer valuable insights for the rational design of non-precious-metal oxide catalysts for O<sub>2</sub> activation and related oxidation reactions through strategic manipulation of metal coordination environments.

## Experimental Section

### Sample preparation

SnO<sub>2</sub> nanosheets were synthesized by direct hydrothermal method in a typical procedure<sup>30</sup>, 0.175 g SnCl<sub>2</sub>·2H<sub>2</sub>O was initially added into 70 mL ethylenediamine. After thorough stirring for 60 min, the mixture was transferred into a 100 mL Teflon-lined autoclave, sealed and heated at 180 °C for 48 h. The system was cooled down to room temperature for 12 h, after which the final product was collected by centrifuging the mixture, washing the collected product with distilled water and absolute ethanol (three times), followed by drying

under vacuum overnight, to provide material suitable for further characterization and catalytic testing. For CO reduction, 0.04 mmol CO (99.999%) was introduced into the glass tube containing 60 mg pretreated and degassed SnO<sub>2</sub> nanosheets on a vacuum line. The glass tube was sealed with flame and then maintained for 0.5 hours at different temperatures. For O<sub>2</sub> oxidation, the CO in the above procedure was replaced by 0.04 mmol O<sub>2</sub> (99.999%) or <sup>17</sup>O<sub>2</sub> (70%, <sup>17</sup>O-abundance). To avoid the exposure of samples to air and water in solid state NMR spectroscopic studies or in-situ DIRFT experiments, material was transferred into a zirconia NMR rotor sealed with a Kel-F end cap or an *in-situ* IR cell in a glove box under dry N<sub>2</sub> atmosphere.

### Characterization

The SEM images were performed by using a FEI Nova 400 Nano. TEM images were obtained on a Tecnai G2 20 TWIN transmission electron microscope with an acceleration voltage of 200 kV. XRD patterns were recorded on a Panalytical X' Pert PRO X-ray diffractometer (40 Kv, 40 mA) using CuKα ( $\lambda=1.5406 \text{ \AA}$ ) radiation.

### Solid-state NMR spectroscopy measurements

<sup>119</sup>Sn MAS NMR experiments were carried out at 9.4T on a Bruker AVANCE III-400 spectrometer with a 3.2 mm double-resonance probe. The resonance frequencies were 148.82 MHz for <sup>119</sup>Sn. Single-pulse excitation <sup>119</sup>Sn MAS experiments were performed on the SnO<sub>2</sub> samples by using a  $\pi/2$  pulse width of 3  $\mu\text{s}$ , a repetition time of 120 s, and a magic angle spinning rate of 12 kHz. The <sup>119</sup>Sn chemical shift was referenced to tetracyclohexyltin at -97.4 ppm. Each <sup>119</sup>Sn spectrum was accumulated for ca. 12 h. <sup>17</sup>O MAS NMR and 2D <sup>1</sup>H-<sup>17</sup>O} D-HMQC MAS NMR experiments were carried out at 18.8T on a Bruker AVANCE III-800 spectrometer with 1.9 mm double-resonance probe and the resonance of frequencies were 108.50 MHz and 800.36 MHz for <sup>17</sup>O and <sup>1</sup>H, respectively. Single pulse <sup>17</sup>O MAS experiments were performed on the SnO<sub>2</sub> samples by using a  $\pi/2$  pulse width of 1.05  $\mu\text{s}$ , a repetition time of 2 s, and a magic angle spinning rate of 35 kHz. The 2D <sup>1</sup>H-<sup>17</sup>O} D-HMQC MAS NMR spectra were collected using SR4 recouplings with  $\tau_{\text{re}} = 0.15 \text{ ms}$  at a spinning speed of 35 kHz, respectively. A total of 128 scans ( $\tau_{\text{re}} = 0.15 \text{ ms}$ ) were collected for the 32 rotor-synchronized t1 increments with recycle delays of 2 s. The <sup>17</sup>O chemical shift was referenced to H<sub>2</sub><sup>17</sup>O at 0 ppm and the <sup>1</sup>H chemical shift was referenced to adamantane at 1.78 ppm. The <sup>17</sup>O MAS NMR spectra were fitted using quadrupolar lineshape with Czsimple model in the DMFIT software. The quadrupolar product parameters were obtained from the <sup>17</sup>O MQMAS NMR spectrum of a fully <sup>17</sup>O-enriched SnO<sub>2</sub> reference sample.

### Catalytic activity measurements

The catalytic properties of CO oxidation for SnO<sub>2</sub> were conducted in a quartz-tube fix-bed reactor using 50 mg catalyst and a mixed gas of 1 vol % CO and 99 vol % dried air at a flow rate of 30 mL/min corresponding to a gas hourly space velocity (GHSV) of 36000 mL h<sup>-1</sup> g<sup>-1</sup>. Typically, the catalyst was heated to the desired temperatures at a rate of 2°C min<sup>-1</sup> and then kept for 30 min until the catalytic reaction reached a steady state. Then, the composition of effluent gas was detected by gas chromatograph (GC 2014, Shimadzu, Japan) equipped with a packed column (TDX-1) and a methane converter in front of a flame ionization detector (FID). Once a cycle was finished, the reactor was cooled to room temperature to start a new cycle. The methane converter is a micro high-temperature furnace (325 °C) with Ni-based catalyst that can fully convert CO and CO<sub>2</sub> into CH<sub>4</sub> for FID detection. The CO conversion was calculated from the change in CO<sub>2</sub> concentration of the inlet and outlet gases.

### In-situ DIRFT experiments

The In-situ DIRFT experiments were performed on a Thermo Scientific Nicolet Is 50 instrument. The SnO<sub>2</sub> nanosheets mixed with 90% KBr was packed into the in situ FTIR cell and degassed with a pressure below 10<sup>-3</sup> Pa. CO (5 kPa) was introduced in the cell and heated at 220 °C for 20 min. The cell was degassed and recharged by O<sub>2</sub> (5 kPa) when it was cooled to room temperature. After that the cell was heated at 220 °C for

another 20 min. The DRIFT spectra during the heating period were recorded by a mercury-cadmium-telluride (MCT) detector with 16 scans at 4 cm<sup>-1</sup> resolution. KBr was used for collecting the background spectrum.

## Acknowledgements

This work was supported by the National Natural Science Foundation of China (grants 22272185, 22225205, 22320102002 and 22127801), the Magnetic Resonance Technology Alliance of the Chinese Academy of Sciences (2021gzl004), the Strategic Priority Research Program of the Chinese Academy of Sciences (XDB0540000), Hubei International Scientific and Technological Cooperation program (2022EHB021), the Natural Science Foundation of Hubei Province of China (S22H120101), and International Science & Technology Cooperation Base for Sustainable Catalysis and Magnetic Resonance (SH2303)

## References

1. Shelef, M.; McCabe, R. W. *Catal. Today*, **2000**, 62, 35-50.  
[http://doi.org/10.1016/S0920-5861\(00\)00407-7](http://doi.org/10.1016/S0920-5861(00)00407-7)
2. Twigg, M. V. *Appl. Catal., B*, **2007**, 70, 2-15.  
<http://doi.org/10.1016/j.apcatb.2006.02.029>
3. Steele, B. C. H.; Heinzel, A. *Nature*, **2001**, 414, 345-352.  
<http://doi.org/10.1038/35104620>
4. Haruta, M.; Kobayashi, T.; Sano, H.; Yamada, N. *Chem. Lett.*, **1987**, 16, 405-408.  
<https://doi.org/10.1246/cl.1987.405>
5. Haruta, M.; Yamada, N.; Kobayashi, T.; Iijima, S. *J. Catal.*, **1989**, 115, 301-309.  
[http://doi.org/10.1016/0021-9517\(89\)90034-1](http://doi.org/10.1016/0021-9517(89)90034-1)
6. Lou, Y.; Cai, Y.; Hu, W.; Wang, L.; Dai, Q.; Zhan, W.; Guo, Y.; Hu, P.; Cao, X.-M.; Liu, J.; Guo, Y. *ACS. Catal.*, **2020**, 10, 6094-6101.  
<http://doi.org/10.1021/acscatal.0c01303>
7. Maurer, F.; Jelic, J.; Wang, J.; Gänzler, A.; Dolcet, P.; Wöll, C.; Wang, Y.; Studt, F.; Casapu, M.; Grunwaldt, J. D. *Nat. Catal.*, **2020**, 3, 824-833.  
<http://doi.org/10.1038/s41929-020-00508-7>
8. Kistler, J. D.; Chotigkrai, N.; Xu, P.; Enderle, B.; Praserttham, P.; Chen, C. Y.; Browning, N. D.; Gates, B. C. *Angew. Chem. Int. Ed.*, **2014**, 53, 8904-8907.  
<http://doi.org/10.1002/ange.201403353>
9. Chen, Y.; Feng, Y.; Li, L.; Liu, J.; Pan, X.; Liu, W.; Wei, F.; Cui, Y.; Qiao, B.; Sun, X.; Li, X.; Lin, J.; Lin, S.; Wang, X.; Zhang, T. *ACS. Catal.*, **2020**, 10, 8815-8824.  
<http://doi.org/10.1021/acscatal.0c02253>
10. Ding, K.; Gulec, A.; Johnson, A. M.; Schweitzer, N. M.; Stucky, G. D.; Marks, L. D.; Stair, P. C. *Science*, **2015**, 350, 189-192.  
<http://doi.org/10.1126/science.aac6368>
11. Su, Y. Q.; Filot, I. A. W.; Liu, J. X.; Hensen, E. J. M. *ACS. Catal.*, **2018**, 8, 75-80.  
<http://doi.org/10.1021/acscatal.7b03295>

12. Gustafson, J.; Balmes, O.; Zhang, C.; Shipilin, M.; Schaefer, A.; Hagman, B.; Merte, L. R.; Martin, N. M.; Carlsson, P. A.; Jankowski, M.; Crumlin, E. J.; Lundgren, E. *ACS. Catal.*, **2018**, 8, 4438-4445.  
<http://doi.org/10.1021/acscatal.8b00498>
13. Haibach, M. C.; Shekhar, S.; Ahmed, T. S.; Ickes, A. R. *Org. Process Res. Dev.*, **2023**, 27, 423-447.  
<http://doi.org/10.1021/acs.oprd.0c00104>
14. Gewirth, A. A.; Varnell, J. A.; DiAscro, A. M. *Chem. Rev.*, **2018**, 118, 2313-2339.  
<http://doi.org/10.1021/acs.chemrev.7b00335>
15. Zhu, C. Z.; Li, H.; Fu, S. F.; Du, D.; Lin, Y. H. *Chem. Soc. Rev.*, **2016**, 45, 517-531.  
<http://doi.org/10.1039/c5cs00670h>
16. Li, D. Z.; Liu, H.; Feng, L. G. *Energy Fuels*, **2020**, 34, 13491-13522.  
<http://doi.org/10.1021/acs.energyfuels.0c03084>
17. Singer, R. A.; Monfette, S.; Bernhardson, D. J.; Tcyrulnikov, S.; Hubbell, A. K.; Hansen, E. C. *Org. Process Res. Dev.*, **2021**, 25, 1802-1815.  
<http://doi.org/10.1021/acs.oprd.0c00104>
18. Yao, Z. C.; Tang, T.; Hu, J. S.; Wan, L. J. *Energy Fuels*, **2021**, 35, 6380-6401.  
<http://doi.org/10.1021/acs.energyfuels.1c00275>
19. Liu, H. R.; Shi, S. R.; Wang, Z. H.; Han, Y. H.; Huang, W. *Small*, **2022**, 18.  
<http://doi.org/10.1002/smll.202103747>
20. Xie, X.; Li, Y.; Liu, Z. Q.; Haruta, M.; Shen, W. *Nature*, **2009**, 458, 746-749.  
<http://doi.org/10.1038/nature07877>
21. Qi, G.; Xu, J.; Su, J.; Chen, J.; Wang, X.; Deng, F. *J. Am. Chem. Soc.*, **2013**, 135, 6762-6765.  
<http://doi.org/10.1021/ja400757c>
22. Fu, Q.; Li, W. X.; Yao, Y. X.; Liu, H. Y.; Su, H. Y.; Ma, D.; Gu, X. K.; Chen, L. M.; Wang, Z.; Zhang, H.; Wang, B.; Bao, X. H. *Science*, **2010**, 328, 1141-1144.  
<http://doi.org/10.1126/science.1188267>
23. Kida, T.; Fujiyama, S.; Suematsu, K.; Yuasa, M.; Shimano, K. *J. Phys. Chem. C*, **2013**, 117, 17574-17582.  
<http://doi.org/10.1021/jp4045226>
24. Bae, J.; Kim, J.; Jeong, H.; Lee, H. *Catal. Sci. Technol.*, **2018**, 8, 782-789.  
<http://doi.org/10.1039/c7cy02108a>
25. Inomata, Y.; Albrecht, K.; Yamamoto, K. *ACS. Catal.*, **2017**, 8, 451-456.  
<http://doi.org/10.1021/acscatal.7b02981>
26. Kocemba, I.; Rynkowski, J. M. *Catal. Today*, **2011**, 169, 192-199.  
<http://doi.org/10.1016/j.cattod.2010.09.015>
27. Jimenez-Morales, I.; Haidar, F.; Cavaliere, S.; Jones D.; Roziere, J. *ACS. Catal.*, **2020**, 10, 10399-10411.  
<http://doi.org/10.1021/acscatal.0c02220>
28. Chen, X. Q.; Li, L. P.; Zhang, Y. L.; Xu, Y. S.; Li, G. S. *RSC. Adv.*, **2016**, 6, 83848-83855.  
<http://doi.org/10.1039/c6ra15932j>
29. Peng, H.; Peng, Y.; Xu, X.; Fang, X.; Liu, Y.; Cai, J.; Wang, X. *Chinese J. Catal.*, **2015**, 36, 2004-2010.  
[http://doi.org/10.1016/s1872-2067\(15\)60926-3](http://doi.org/10.1016/s1872-2067(15)60926-3)
30. Sun, Y.; Lei, F.; Gao, S.; Pan, B.; Zhou, J.; Xie, Y. *Angew. Chem. Int. Ed.*, **2013**, 52, 10569-10572.  
<http://doi.org/10.1002/anie.201305530>
31. Wang, X.; Xiao, L.; Peng, H.; Liu, W.; Xu, X. *J. Mater. Chem. A*, **2014**, 2, 5616-5619.  
<http://doi.org/10.1039/c3ta15109c>
32. Chmelka, B. F. *J. Magn. Reson.*, **2019**, 306, 91-97.

- <http://doi.org/10.1016/j.jmr.2019.07.051>
33. Hunger, M. *Catal. Rev.*, **1997**, 39, 345-393.  
<http://doi.org/10.1080/01614949708007100>
34. Qi, G. D.; Wang, Q.; Xu, J.; Deng, F. *Chem. Soc. Rev.*, **2021**, 50, 8382-8399.  
<http://doi.org/10.1039/d0cs01130d>
35. Harris, R. K.; Becker, E. D.; de Menezes, S. M. C.; Goodfellow, R.; Granger, P. *Magn. Reson. Chem.*, **2002**, 40, 489-505.  
<http://doi.org/10.1006/snmr.2002.0063>
36. Harris, R. K.; Packer, K. J.; Reams, P. J. *Magn. Reson.*, **1985**, 61, 564-566.  
[http://doi.org/10.1016/0022-2364\(85\)90199-4](http://doi.org/10.1016/0022-2364(85)90199-4)
37. Harris, R. K.; Packer, K. J.; Reams, P.; Sebald, A. J. *Magn. Reson.*, **1987**, 72, 385-387.  
[http://doi.org/10.1016/0022-2364\(87\)90305-2](http://doi.org/10.1016/0022-2364(87)90305-2)
38. Harris, R. K.; Mitchell, T. N.; Nesbitt, G. J. *Magn. Reson. Chem.*, **1985**, 23, 1080-1081.  
<http://doi.org/10.1002/mrc.1260231211>
39. Harris, R. K.; Sebald, A. *Magn. Reson. Chem.*, **1987**, 25, 1058-1062.  
<http://doi.org/10.1002/mrc.1260251208>
40. Cossement, C.; Darville, J.; Gilles, J. M.; Nagy, J. B.; Fernandez, C.; Amoureux, J. P. *Magn. Reson. Chem.*, **1992**, 30, 263-270.  
<http://doi.org/10.1002/mrc.1260300313>
41. Chen, J.; Wu, X. P.; Shen, L.; Li, Y.; Wu, D.; Ding, W.; Gong, X. Q.; Lin, M.; Peng, L. *Chem. Phys. Lett.*, **2016**, 643, 126-130.  
<http://doi.org/10.1016/j.cplett.2015.11.035>
42. Qi, G.; Wang, Q.; Xu, J.; Wu, Q.; Wang, C.; Zhao, X.; Meng, X.; Xiao, F.; Deng, F. *Commun. Chem.*, **2018**, 1, 22.  
<http://doi.org/10.1038/s42004-018-0023-1>
43. Li, W.; Wang, Q.; Xu, J.; Aussenac, F.; Qi, G.; Zhao, X.; Gao, P.; Wang, C.; Deng, F. *Phys. Chem. Chem. Phys.*, **2018**, 20, 17218-17225.  
<http://doi.org/10.1039/c8cp03132k>
44. Wang, Q.; Li, W. Z.; Hung, I.; Mentink-Vigier, F.; Wang, X. L.; Qi, G. D.; Wang, X.; Gan, Z. H.; Xu, J.; Deng, F. *Nat. Commun.*, **2020**, 11, 3620.  
<http://doi.org/10.1038/s41467-020-17470-4>
45. Li, Y.; Wu, X. P.; Jiang N.; Lin, M.; Shen, L.; Sun, H.; Wang, Y.; Wang, M.; Ke, X.; Yu, Z.; Gao, F.; Dong, L.; Guo, X.; Hou, W.; Ding, W.; Gong, X. Q.; Grey, C. P.; Peng, L. *Nat. Commun.*, **2017**, 8, 581.  
<http://doi.org/10.1038/s41467-017-00603-7>
46. Li, G. X.; Li, S. D.; Han, Z. K.; Zou, C.; Wu, H. L.; Yuan, W. T.; Zhu, B. E.; Gao, Y.; Yang, H. S.; Zhang, Z.; Wang, Y. *Nano. Lett.*, **2021**, 21, 7309-7316.  
<http://doi.org/10.1021/acs.nanolett.1c02501>
47. Lu, Z.; Ma, D.; Yang, L.; Wang, X.; Xu, G.; Yang, Z. *Phys. Chem. Chem. Phys.*, **2014**, 16, 12488-12494.  
<http://doi.org/10.1039/c4cp00540f>
48. Wang, J.; Su, Y.; Xu, J.; Ye, C.; Deng, F. *Phys. Chem. Chem. Phys.*, **2006**, 8, 2378-2384.  
<http://doi.org/10.1039/b516833c>
49. Zhao, Y.; Teng, B. T.; Wen, X. D.; Zhao, Y.; Chen, Q. P.; Zhao, L. H.; Luo, M. F. *J. Phys. Chem. C.*, **2012**, 116, 15986-15991.  
<http://doi.org/10.1021/jp3016326>



50. Fang, H. C.; Li, Z. H.; Fan, K. N. *Phys. Chem. Chem. Phys.*, **2011**, *13*, 13358-13369.  
<http://doi.org/10.1039/c1cp21160a>
51. Liu, B.; Li, W. P.; Song, W. Y.; Liu, J. *Phys. Chem. Chem. Phys.*, **2018**, *20*, 16045-16059.  
<http://doi.org/10.1039/c8cp01694a>
52. Liu, Y. J.; Lin, L.; Yu, L.; Mu, R. T.; Fu, Q. *J. Phys. Chem. Lett.*, **2023**, *14*, 9780-9786.  
<http://doi.org/10.1021/acs.jpcllett.3c02247>

This paper is an open access article distributed under the terms of the Creative Commons Attribution (CC BY) license (<http://creativecommons.org/licenses/by/4.0/>)